Supplementary Information

Bi Catalysts Supported on GaN Nanowires toward Efficient Photoelectrochemical CO_2 Reduction

Wan Jae Dong,[1,2,‡] Ishtiaque Ahmed Navid,[1‡] Yixin Xiao,[1] Tae Hyung Lee,[3] Jin Wook Lim,[2] Donghwa Lee,[4] Ho Won Jang,[3,5*] Jong-Lam Lee,[2*] and Zetian Mi[1*]

[1] Department of Electrical Engineering and Computer Science, University of Michigan, 1301 Beal Avenue, Ann Arbor, MI 48109, USA

[2] Department of Materials Science and Engineering, Pohang University of Science and Technology (POSTECH), Pohang 37673, Korea.

[3] Department of Materials Science and Engineering, Research Institute of Advanced Materials, Seoul National University, Seoul 08826, Korea

[4] Division of Advanced Materials Science, Pohang University of Science and Technology (POSTECH), Pohang 37673, Korea

[5] Advanced Institute of Convergence Technology, Seoul National University, Suwon 16229, Korea

[*]*E-mail: ztmi@umich.edu, jllee@postech.ac.kr, hwjang@snu.ac.kr*

[‡]W. J. Dong, I. A. Navid contributed equally to this work.

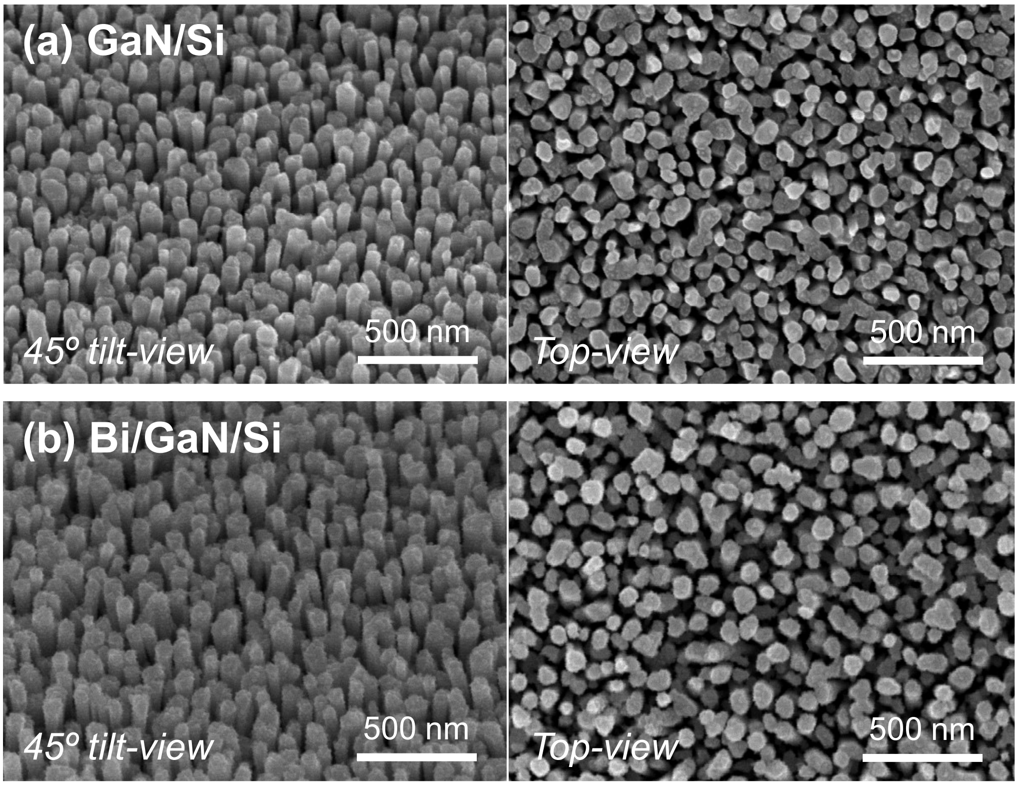

Fig. S1. Low-magnification scanning electron microscopy (SEM) images of (a) GaN/Si and (b) Bi/GaN/Si photoelectrodes.

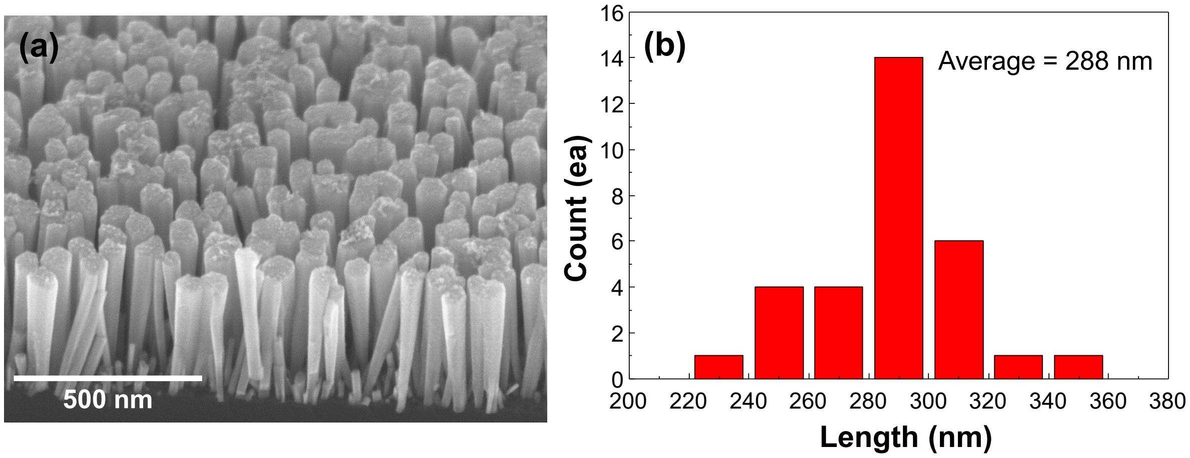

Fig. S2. (a) 45-degree-tilt-view SEM image of GaN NWs grown on planar Si wafer. (b) Measured lengths of GaN NWs.

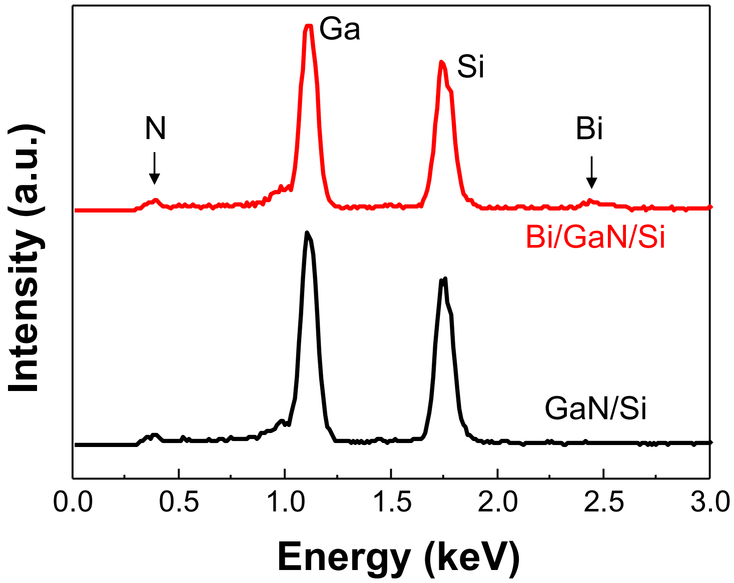

Fig. S3. Energy dispersive X-ray spectroscope (EDS) spectra of GaN/Si (black) and Bi/GaN/Si (red).

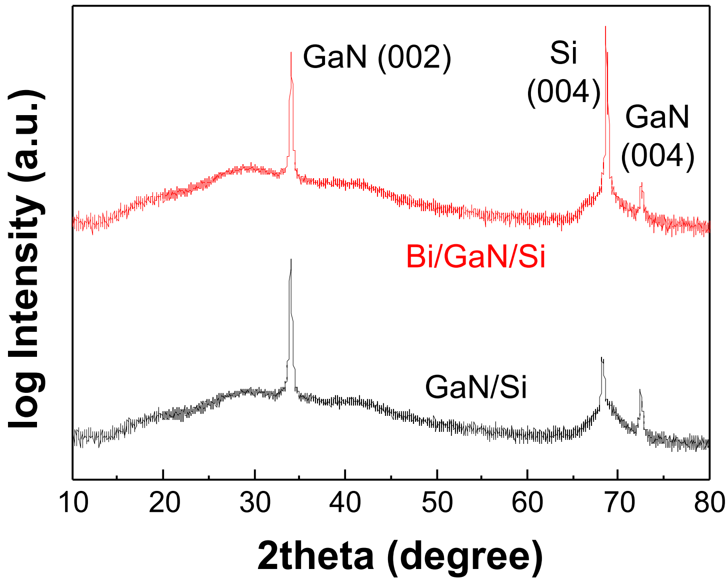

Fig. S4. X-ray diffraction patterns of GaN/Si (black) and Bi/GaN/Si (red).

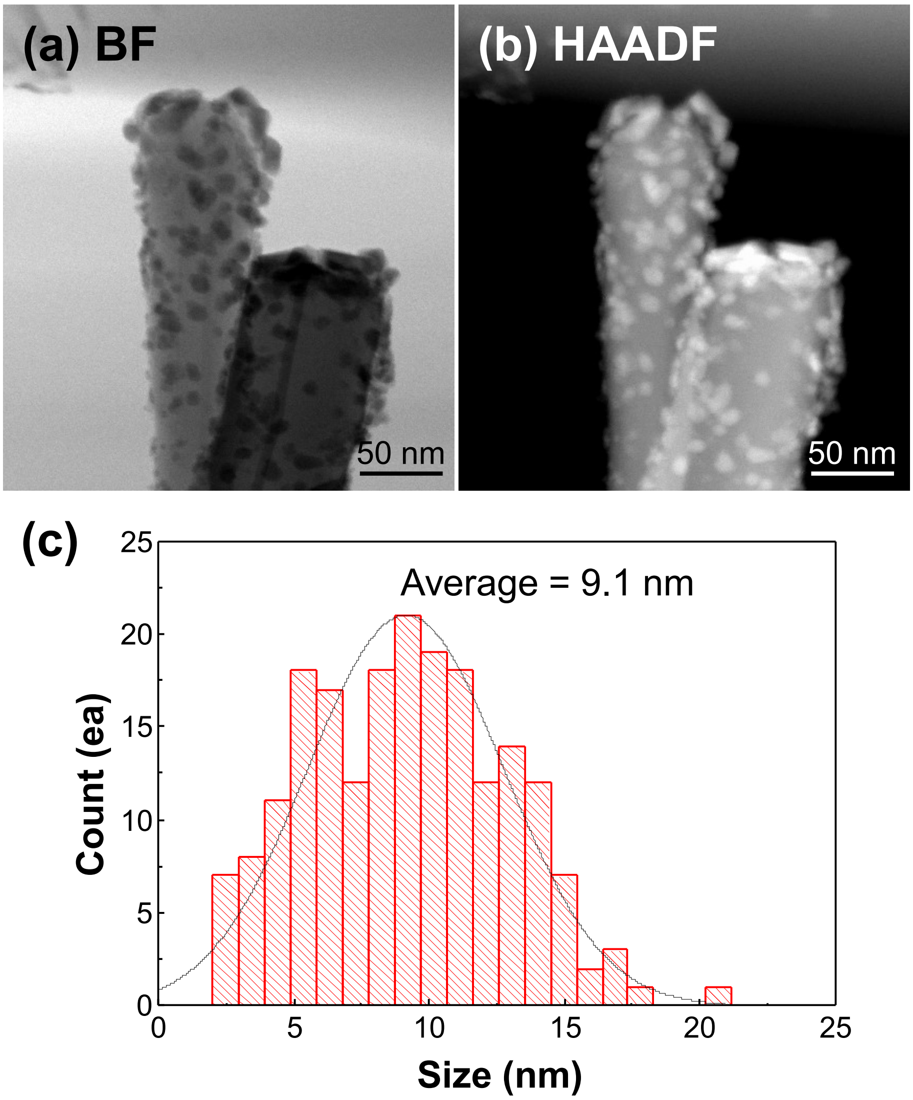

Fig. S5. (a) Bright-field (BF) and (b) high-angle annular dark-field (HAADF) scanning transmission electron microscope (STEM) images of Bi/GaN NWs. (c) Histogram of particle size distribution for Bi NPs. The size was calculated by a computing-based image analyzer (Leopard).

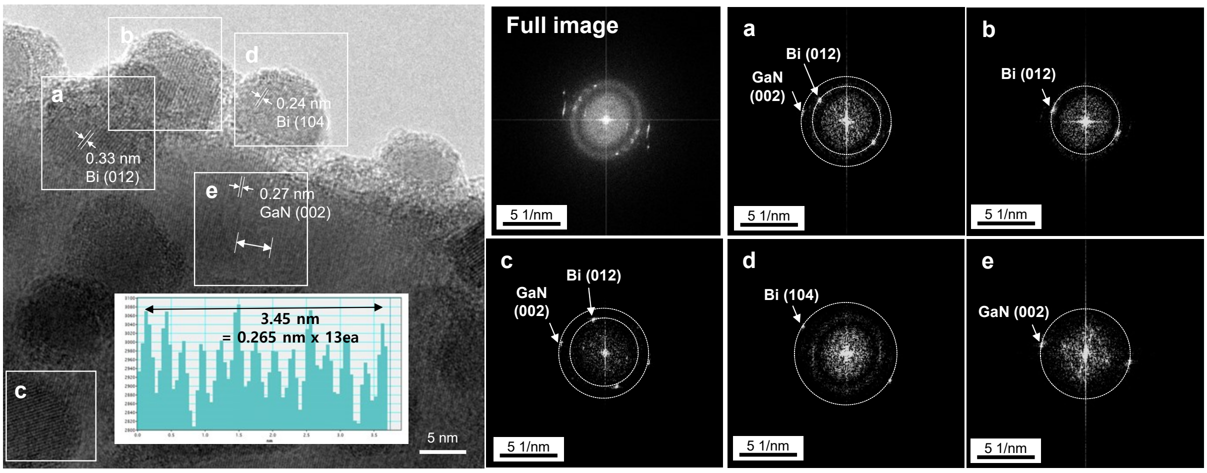

Fig. S6. High-resolution TEM image of Bi/GaN NW and selected area electron diffraction patterns at each region indicated by a-e. The inset shows lattice spacing of GaN (002) plane.

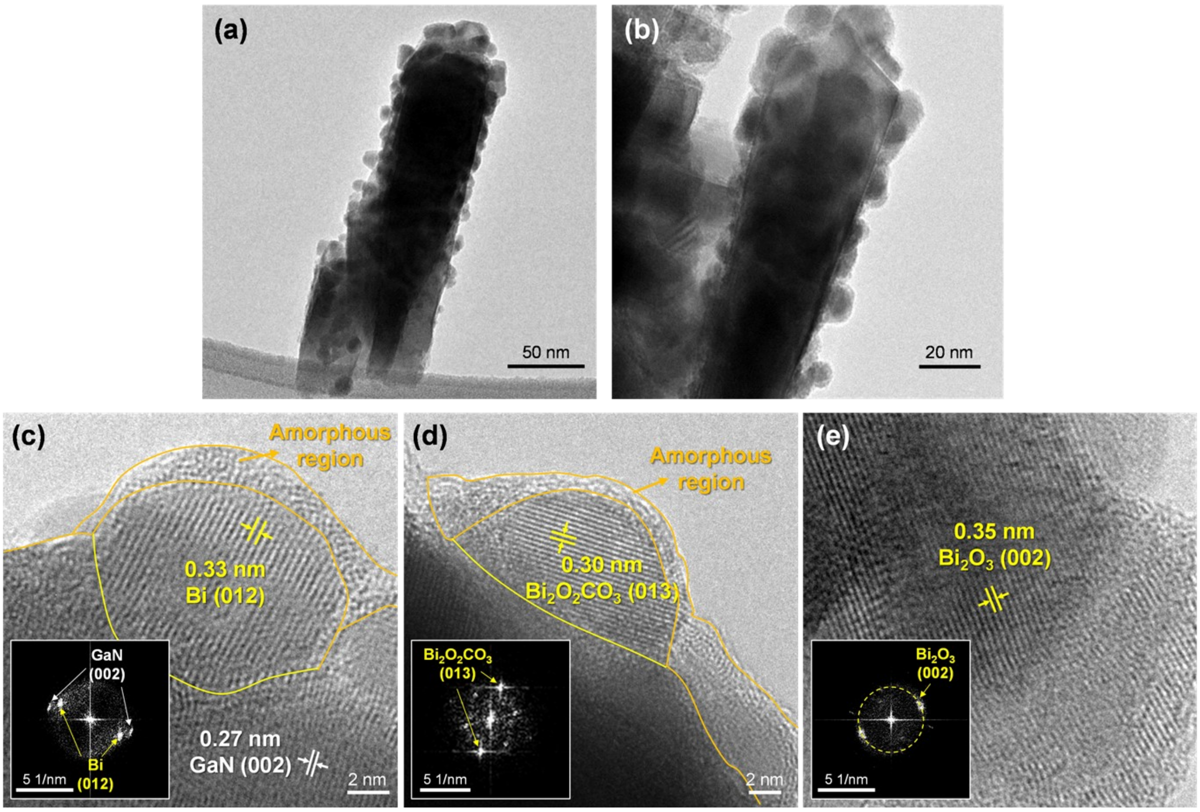

Fig. S7. (a,b) TEM images of Bi NPs and GaN NWs after CO_2 RR for 20 min at -0.4 V_{RHE} in 0.1 M $KHCO_3$. (c-e) High-resolution TEM images and electron diffraction patterns of Bi/GaN after CO_2 RR. Bi (012) plane with a lattice spacing of 0.33 nm, $Bi_2O_2CO_3$ (013) plane with a lattice spacing of 0.30 nm, and Bi_2O_3 (002) plane with a lattice spacing of 0.35 nm were observed.

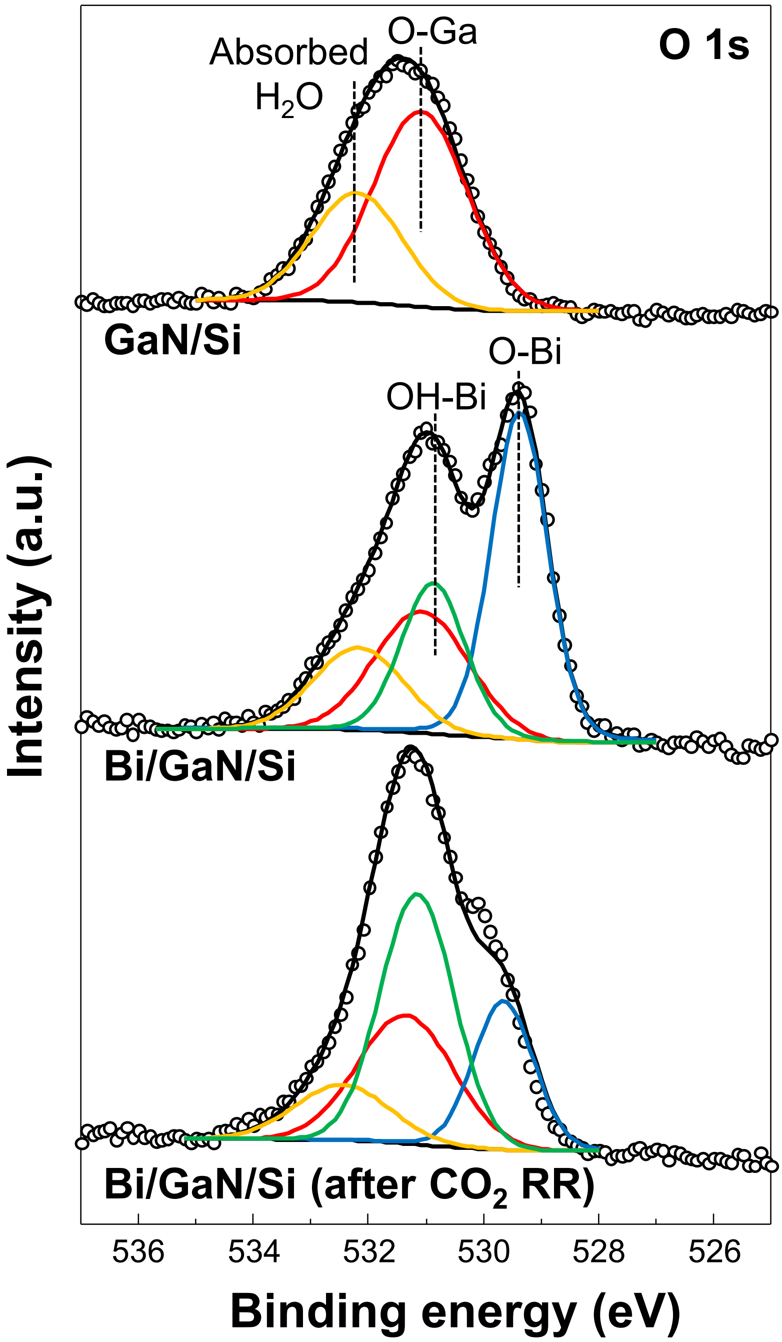

Fig. S8. O 1s X-ray photoelectron spectroscope (XPS) spectra of GaN/Si, Bi/GaN/Si, and Bi/GaN/Si after PEC CO_2 reduction reaction at -0.4 V_{RHE} for 20 min.

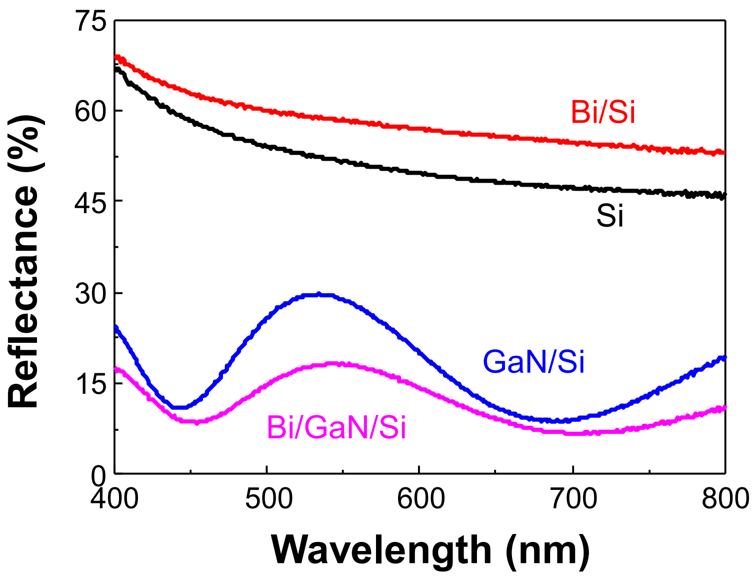

Fig. S9. Optical reflectance spectra of Si, Bi/Si, GaN/Si, and Bi/GaN/Si.

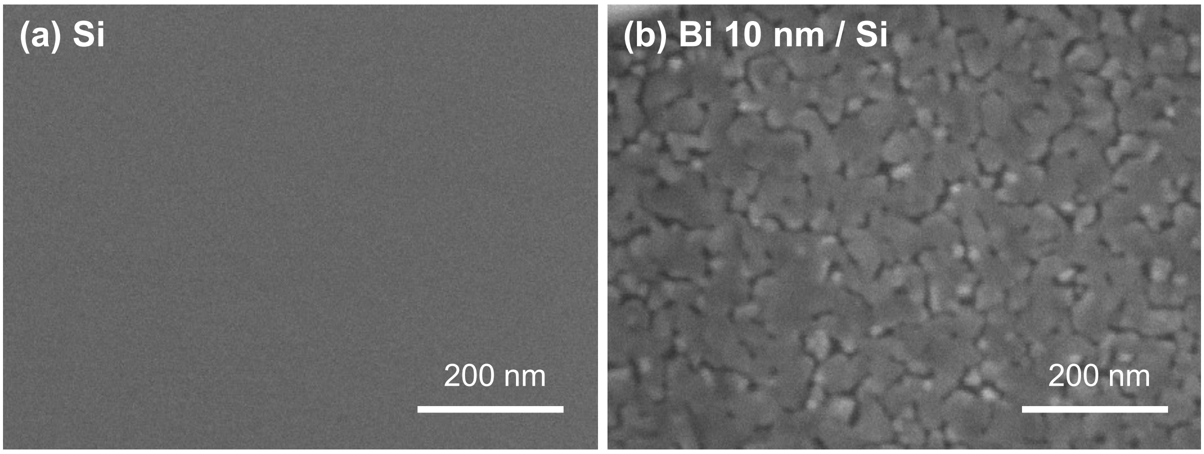

Fig. S10. Top-view SEM images of (a) Si wafer and (b) Bi 10 nm-deposited Si.

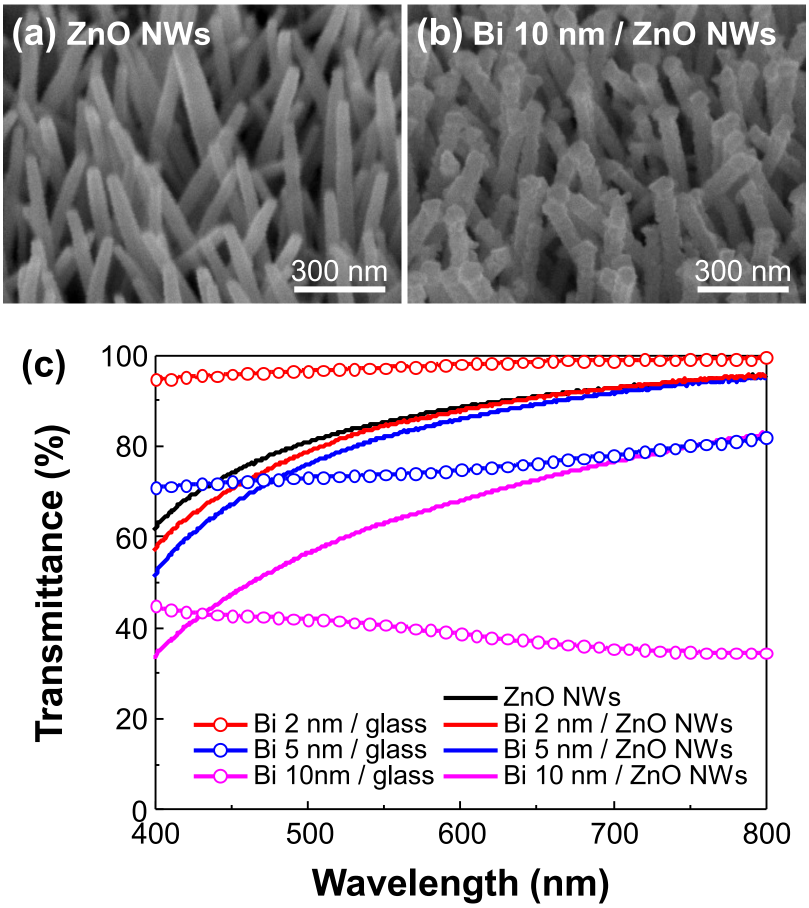

Fig. S11. 45°-tilt-view SEM images of (a) ZnO nanowires (NWs) and (b) Bi 10 nm-deposited ZnO NWs. ZnO NWs were nearly vertically grown on glass substrates. (c) Optical transmittance of Bi/glass and Bi/ZnO NWs/glass with Bi thicknesses of 2, 5, and 10 nm. Compared to Bi films deposited on planar glass substrate, Bi NPs formed on ZnO NWs showed better optical transmittance.

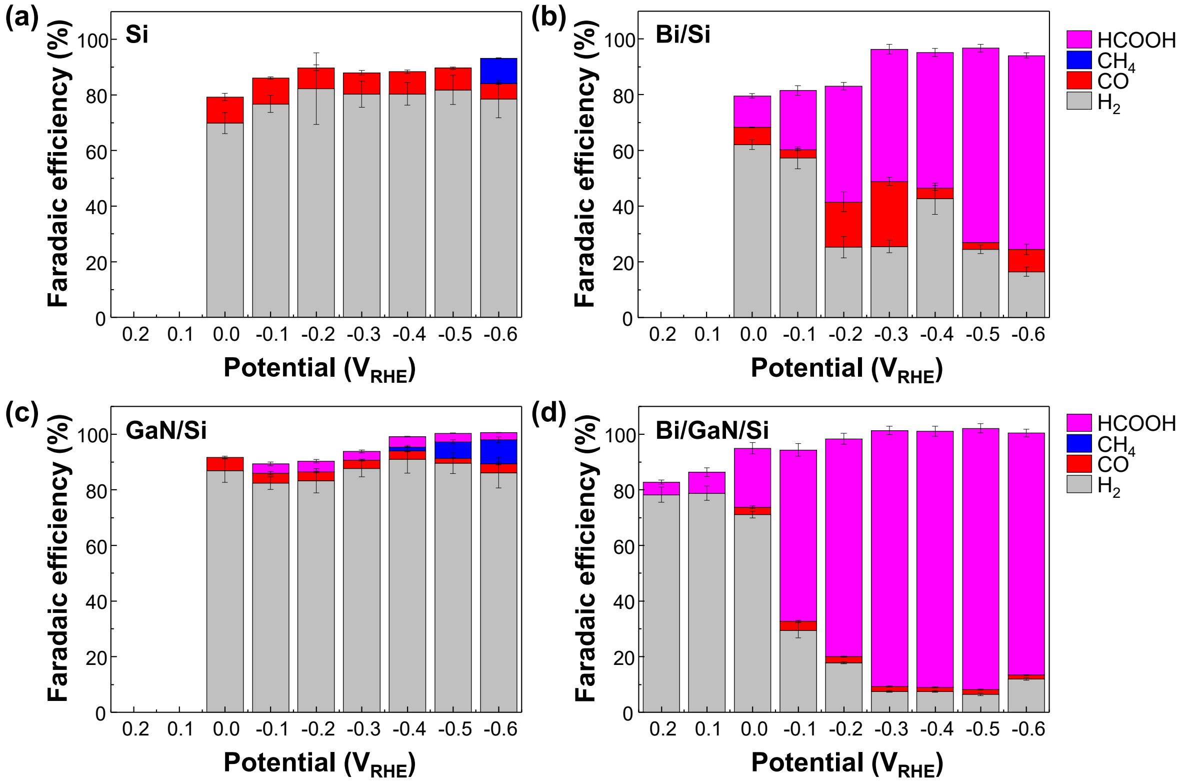

Fig. S12. Faradaic efficiency of photoelectrochemical CO_2 reduction reaction products for (a) Si, (b) Bi/Si, (c) GaN/Si, and (d) Bi/GaN/Si. The measurements were conducted in CO_2-purged 0.1 M $KHCO_3$ electrolyte under 100 mW/cm^2 light illumination.

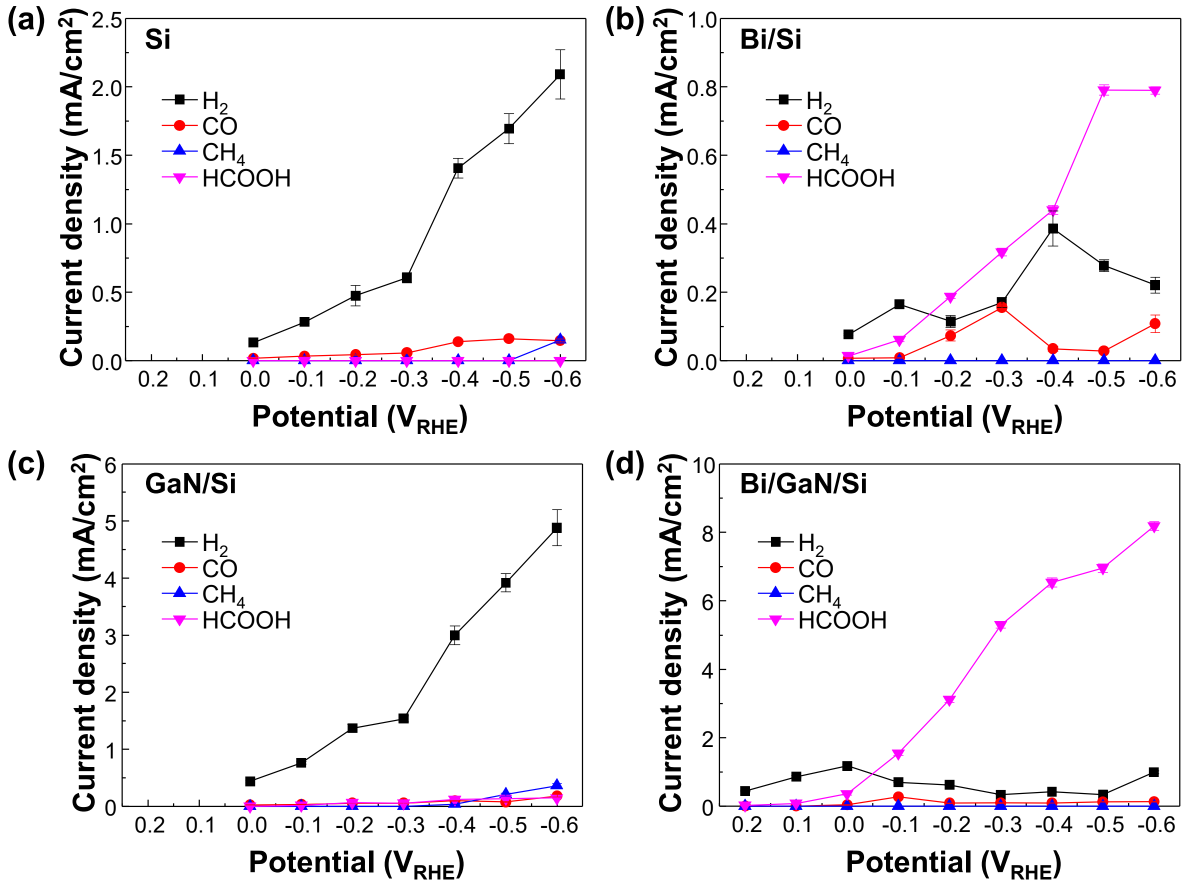

Fig. S13. Partial current density of photoelectrochemical CO_2 reduction reaction products for (a) Si, (b) Bi/Si, (c) GaN/Si, and (d) Bi/GaN/Si.

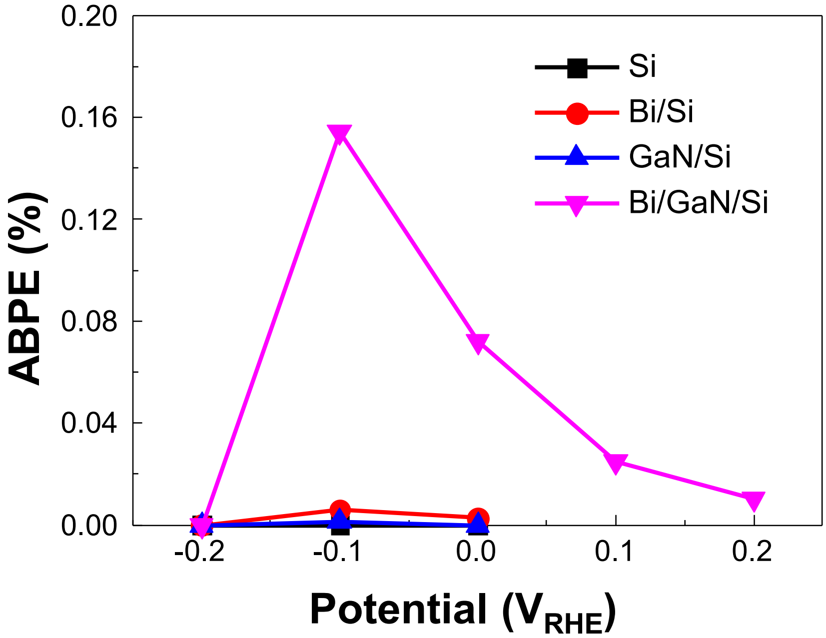

Fig. S14. Applied bias photon-to-current efficiency (ABPE) of photocathodes.

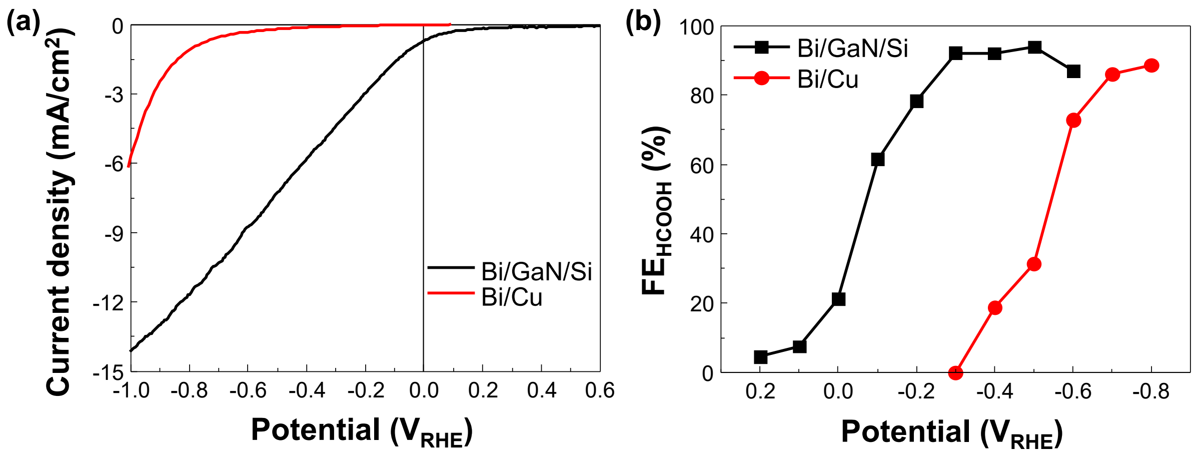

Fig. S15. (a) LSV curves and (b) FE_{HCOOH} of Bi/GaN/Si photocathode and Bi/Cu electrocatalyst measured in CO_2-purged 0.1 M $KHCO_3$ electrolyte.

Bi/Cu electrocatalyst was fabricated by deposition of 10 nm-thick Bi film on Cu foil by thermal evaporation method. In the linear sweep voltammetry curves, it is obvious that Bi/GaN/Si photocathode showed a more positive onset potential and a higher current density than Bi/Cu electrocatalysts (Fig. S15a). Bi/GaN/Si revealed high FE_{HCOOH} = 92.1% at -0.4 V_{RHE} whereas Bi/Cu catalysts exhibited low FE_{HCOOH} = 18.8% at -0.4 V_{RHE} (Fig. S15b).

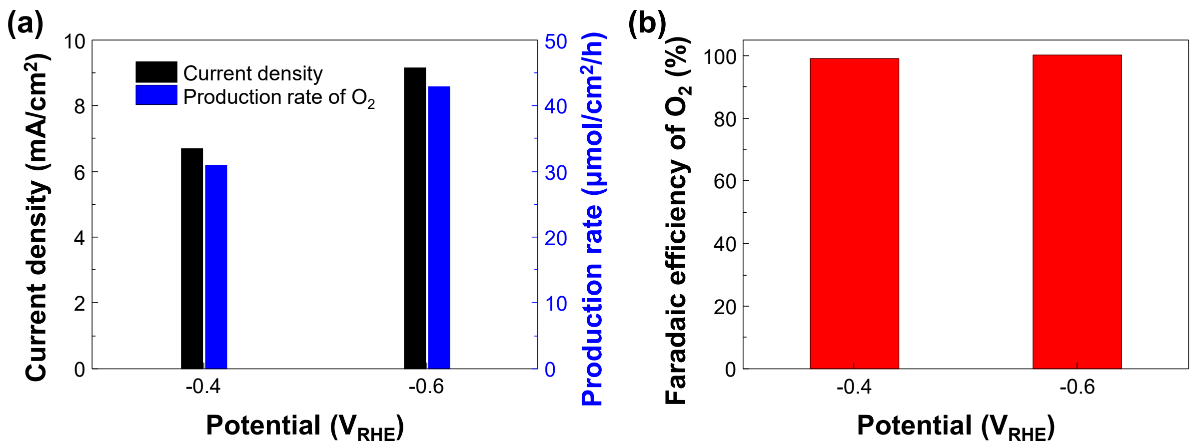

Fig. S16. (a) Measured current density and production rate of O_2 in the anodic reactor. (b) Faradaic efficiency of O_2. When cathodic potentials of -0.4 and -0.6 V_{RHE} were applied to the photocathode for 20 min, the average current densities were 6.68 and 9.17 mA/cm^2 and the O_2 production rates in anodic reactor were 30.9 and 42.9 $\mu mol/cm^2/h$, respectively.

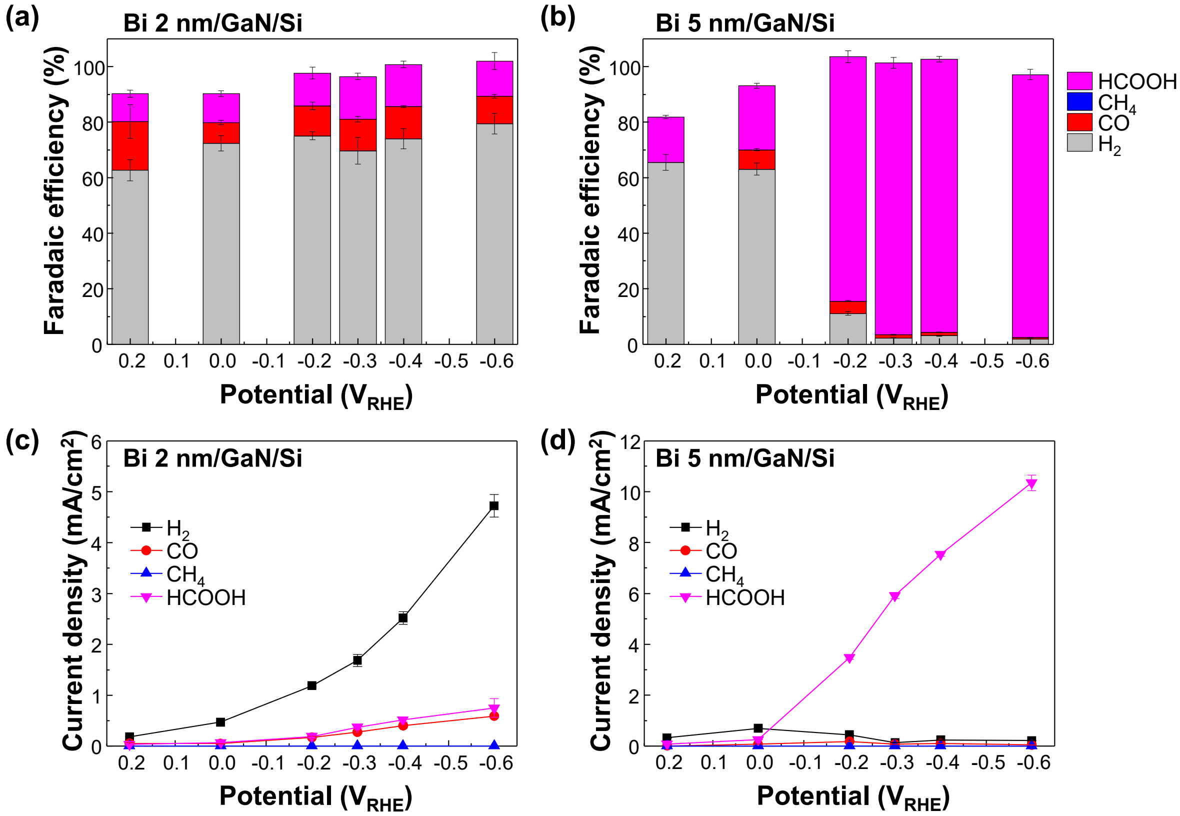

Fig. S17. (a,b) Faradaic efficiency and (c,d) partial current density of PEC CO_2 reduction reaction products for Bi 2 nm/GaN/Si and Bi 5 nm/GaN/Si.

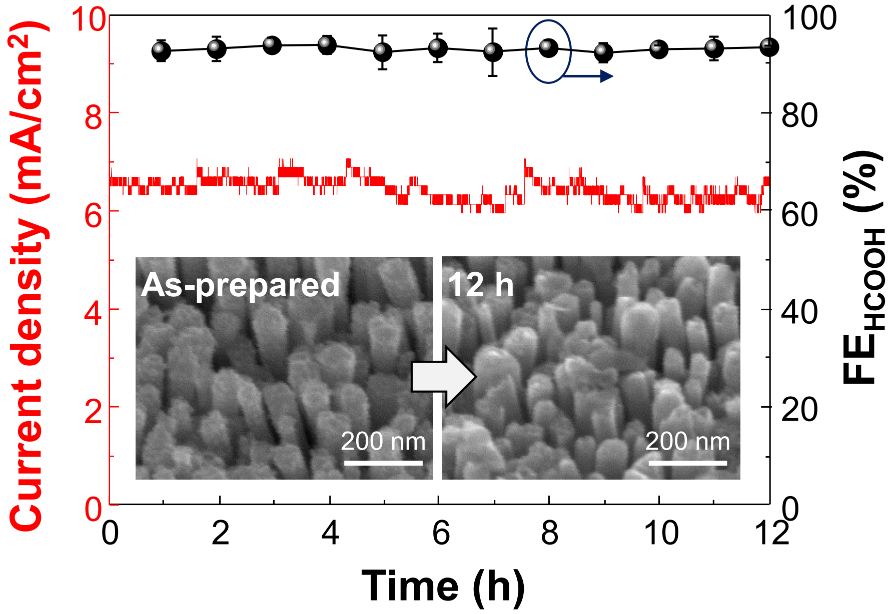

Fig. S18. Stability of Bi/GaN/Si photocathode was evaluated at -0.4 V_{RHE} in 0.1 M $KHCO_3$ electrolyte. Current density (red curve) and FE_{HCOOH} (black symbol) were plotted as a function of reaction time. Inset: SEM images of Bi/GaN/Si before and after 12 h operation.

To evaluate the stability of Bi/GaN/Si photoelectrode, PEC CO_2 RR was performed for 12 h at a constant potential of -0.4 V_{RHE} in CO_2-purged 0.1 M $KHCO_3$ electrolyte. For the current density measurement, CO_2 gas was continuously fed in the electrolyte to prevent the change of the pH value during the reaction. The current density (~6.5 mA/cm^2) was almost constant for 12 h, indicating that the PEC CO_2 RR was stable under long-term operation (Fig. S18). For the FE measurement, the electrolyte was replaced with clean CO_2-purged $KHCO_3$ solution after finishing the reaction for 1 h. Bi/GaN/Si showed high FE_{HCOOH} > 90% for 12 h operation. Also, the morphology of the Bi/GaN/Si did not change after the reaction. It is therefore seen that Bi/GaN/Si is a promising photocathode for PEC CO_2 RR with prolonged stability.

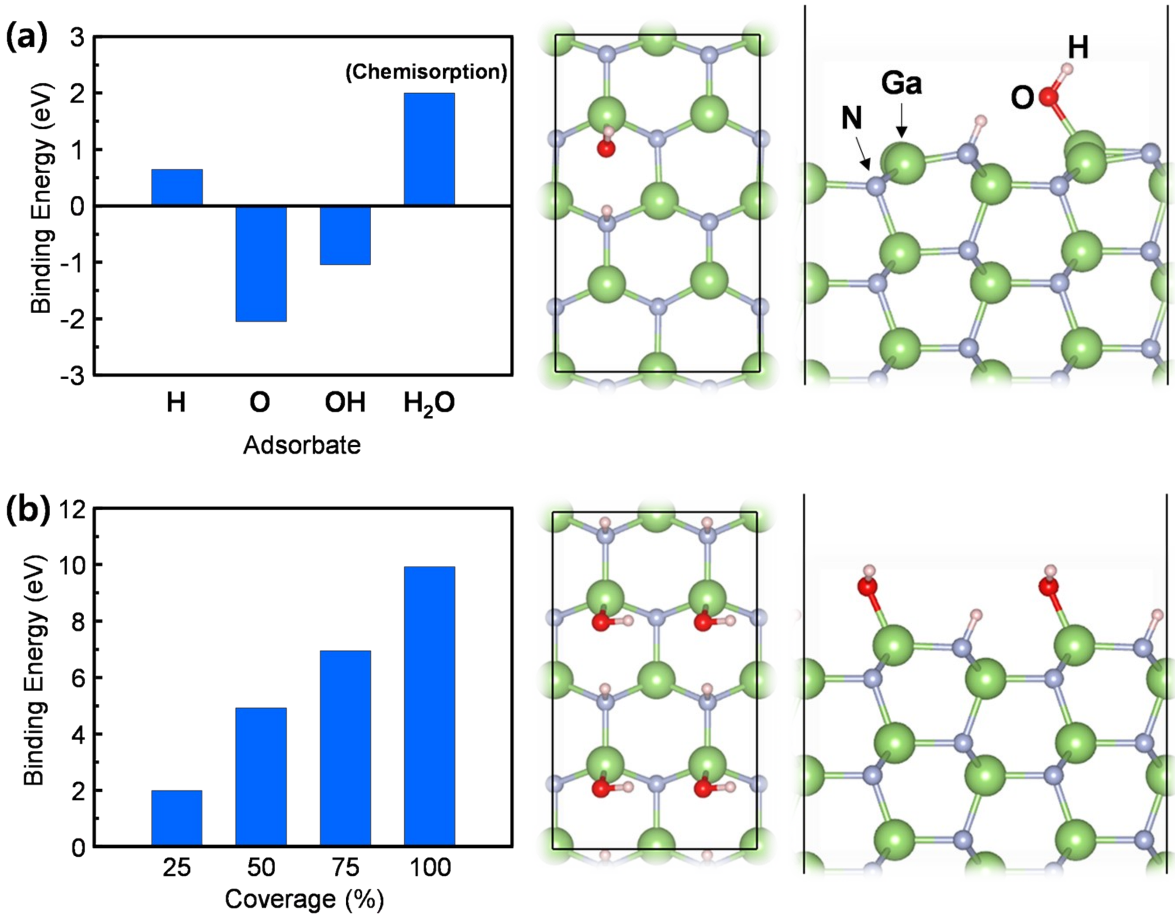

Fig. S19. (a) Calculated binding energy of H, O, OH, and H_2O adsorbates on GaN$(10\bar{1}0)$ and optimized geometry. (b) Coverage-dependent binding energy of H_2O on GaN$(10\bar{1}0)$.

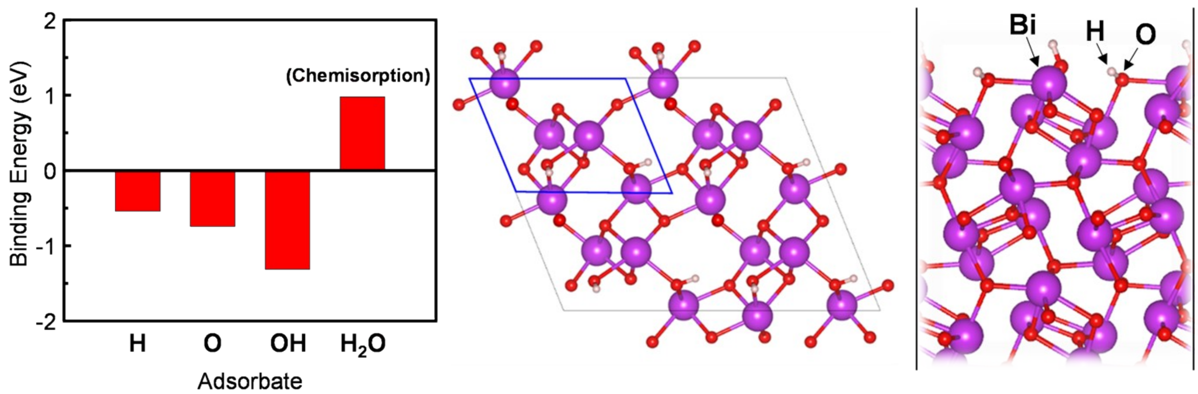

Fig. S20. Calculated binding energy of H, O, OH, and H_2O adsorbates on Bi_2O_3 and optimized geometry.

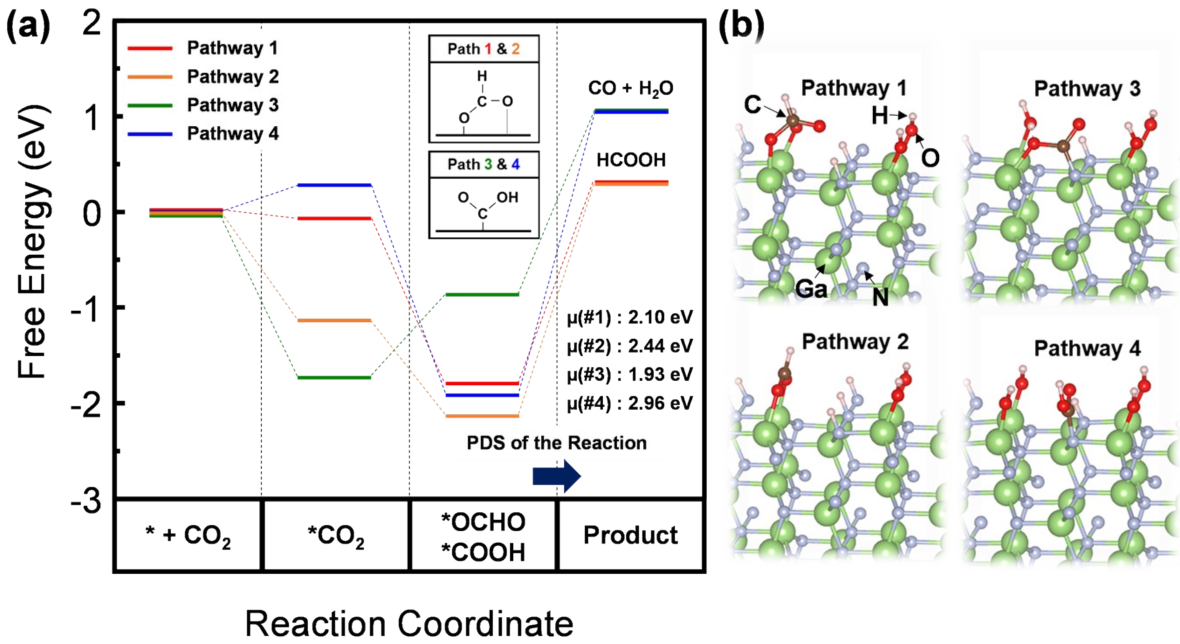

Fig. S21. (a) Free-energy profiles for CO_2 RR to HCOOH and CO on GaN$(10\bar{1}0)$. (b) Optimized geometry of each reaction pathway. *OCHO is the reaction intermediate for HCOOH production via pathway 1 and 2. *COOH is the reaction intermediate for CO production via pathway 3 and 4.

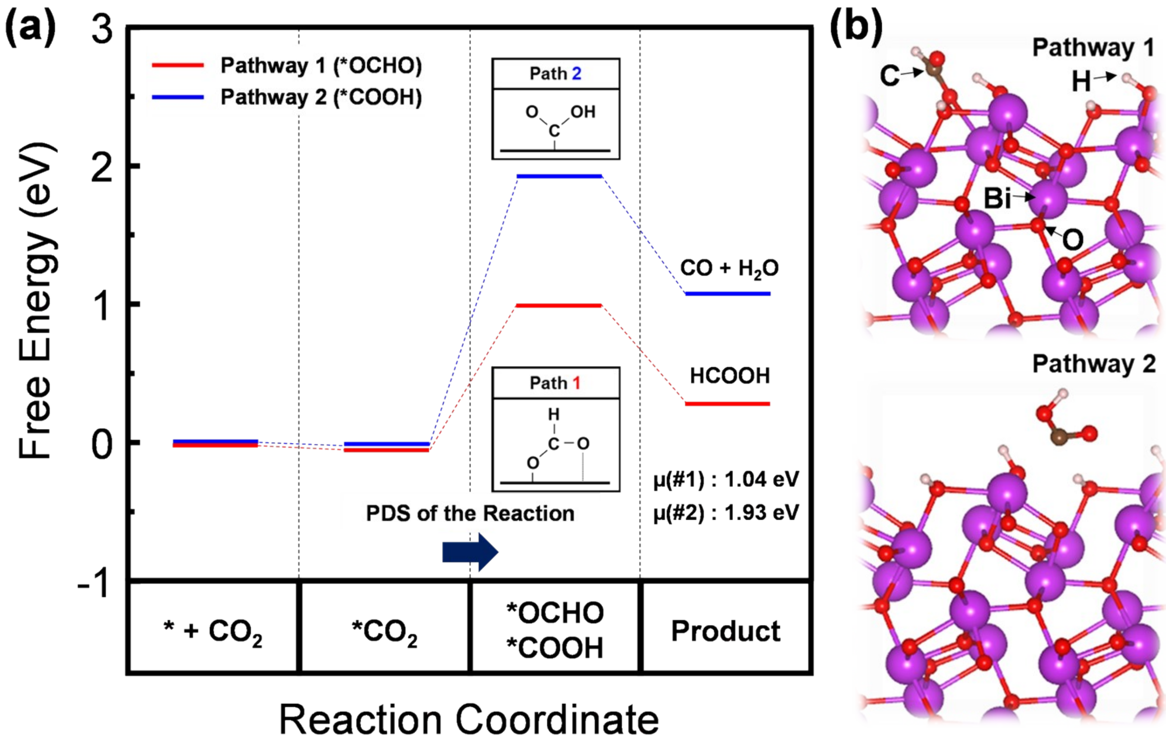

Fig. S22. (a) Free-energy profiles for CO_2 RR to HCOOH and CO on Bi_2O_3. (b) Optimized geometry of each reaction pathway.

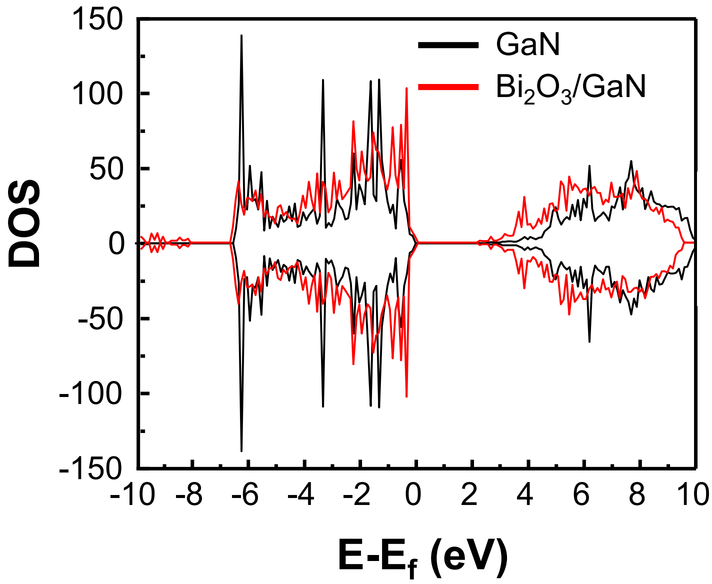

Fig. S23. Calculated density of states for GaN and Bi_2O_3/GaN$(10\bar{1}0)$. DOS plots were mainly aligned based on the partial density of states (PDOS) of Ga atom at the fixed region to mimic the bulk-like GaN.

Table S1. Summary of PEC CO_2 RR performance.

Electrodes	Potential (V_{RHE})	FE_{HCOOH} (%)	FE_{H2} (%)	FE_{CO} (%)	FE_{CH4} (%)	j_{HCOOH} (mA/cm^2)	j_{H2} (mA/cm^2)	j_{CO} (mA/cm^2)	j_{CH4} (mA/cm^2)
Si	0	0.0±0.0	69.9±3.9	9.3±1.3	0.0±0.0	0.00±0.00	0.13±0.01	0.02±0.00	0.00±0.00
	-0.1	0.0±0.0	76.8±3.1	9.3±0.4	0.0±0.0	0.00±0.00	0.28±0.01	0.03±0.00	0.00±0.00
	-0.2	0.0±0.0	82.2±12.9	7.5±1.0	0.0±0.0	0.00±0.00	0.48±0.07	0.04±0.01	0.00±0.00
	-0.3	0.0±0.0	80.3±4.7	7.7±0.8	0.0±0.0	0.00±0.00	0.61±0.04	0.06±0.01	0.00±0.00
	-0.4	0.0±0.0	80.4±4.1	7.9±0.6	0.0±0.0	0.00±0.00	1.41±0.07	0.14±0.01	0.00±0.00
	-0.5	0.0±0.0	81.8±5.3	7.8±0.4	0.0±0.0	0.00±0.00	1.69±0.11	0.16±0.01	0.00±0.00
	-0.6	0.0±0.0	78.6±6.7	5.5±0.4	9.1±0.2	0.00±0.00	2.09±0.18	0.15±0.01	0.15±0.00
Bi 10nm /Si	0	11.3±0.8	62.1±1.7	6.2±0.2	0.0±0.0	0.01±0.00	0.08±0.00	0.01±0.00	0.00±0.00
	-0.1	21.3±1.7	57.3±3.9	2.9±0.4	0.0±0.0	0.06±0.00	0.16±0.01	0.01±0.00	0.00±0.00
	-0.2	41.5±1.4	25.3±3.9	16.2±3.5	0.0±0.0	0.19±0.01	0.11±0.02	0.07±0.02	0.00±0.00
	-0.3	47.5±1.7	25.5±2.2	23.3±1.5	0.0±0.0	0.32±0.01	0.17±0.01	0.16±0.01	0.00±0.00
	-0.4	48.6±1.5	42.7±5.7	3.8±0.8	0.0±0.0	0.44±0.01	0.39±0.05	0.03±0.01	0.00±0.00
	-0.5	69.7±1.4	24.5±1.6	2.5±0.0	0.0±0.0	0.79±0.02	0.28±0.02	0.03±0.00	0.00±0.00
	-0.6	69.6±1.0	16.4±1.7	8.0±1.9	0.0±0.0	0.79±0.01	0.22±0.02	0.11±0.03	0.00±0.00
GaN/Si	0	0.0±0.0	86.9±4.2	4.9±0.4	0.0±0.0	0.00±0.00	0.43±0.02	0.02±0.00	0.00±0.00
	-0.1	3.3±0.7	82.5±2.3	3.5±0.6	0.0±0.0	0.02±0.00	0.76±0.02	0.03±0.01	0.00±0.00
	-0.2	3.8±0.6	83.3±4.3	3.2±0.3	0.0±0.0	0.06±0.01	1.37±0.07	0.05±0.00	0.00±0.00
	-0.3	3.1±0.5	87.7±3.1	3.0±0.3	0.0±0.0	0.05±0.01	1.53±0.05	0.05±0.01	0.00±0.00
	-0.4	3.7±0.1	91.0±5.0	2.9±0.2	1.5±0.0	0.12±0.00	3.00±0.16	0.10±0.01	0.04±0.00
	-0.5	3.1±0.1	89.5±3.7	1.8±0.1	5.9±0.6	0.14±0.00	3.91±0.16	0.08±0.01	0.21±0.02
	-0.6	2.6±0.1	86.2±5.6	3.3±0.4	8.6±1.0	0.14±0.00	4.88±0.32	0.19±0.02	0.36±0.04
Bi 10 nm /GaN/Si	0.2	4.6±0.8	78.2±2.7	0.0±0.0	0.0±0.0	0.03±0.00	0.44±0.02	0.00±0.00	0.00±0.00
	0.1	7.6±1.6	78.8±2.6	0.0±0.0	0.0±0.0	0.08±0.02	0.86±0.03	0.00±0.00	0.00±0.00
	0	21.2±2.0	71.1±1.1	2.6±0.5	0.0±0.0	0.36±0.03	1.17±0.04	0.04±0.01	0.00±0.00
	-0.1	61.6±2.3	29.5±2.7	3.2±0.4	0.0±0.0	1.54±0.06	0.70±0.00	0.28±0.00	0.00±0.00
	-0.2	78.4±1.9	17.8±0.3	2.2±0.2	0.0±0.0	3.12±0.08	0.62±0.02	0.09±0.01	0.00±0.00
	-0.3	92.1±1.5	7.5±0.3	1.7±0.3	0.0±0.0	5.29±0.09	0.33±0.00	0.10±0.01	0.00±0.00
	-0.4	92.1±1.8	7.5±0.3	1.4±0.1	0.0±0.0	6.53±0.13	0.42±0.01	0.09±0.00	0.00±0.00
	-0.5	93.9±1.7	6.5±0.5	1.7±0.2	0.0±0.0	6.95±0.12	0.34±0.00	0.13±0.01	0.00±0.00
	-0.6	87.0±1.3	12.0±0.6	1.4±0.1	0.0±0.0	8.19±0.13	0.99±0.04	0.13±0.01	0.00±0.00
Bi 5 nm /GaN/Si	0.2	16.3±0.6	65.5±2.9	0.0±0.0	0.0±0.0	0.08±0.00	0.32±0.01	0.00±0.00	0.00±0.00
	0	23.1±0.9	63.1±2.1	7.0±0.4	0.0±0.0	0.25±0.01	0.69±0.02	0.08±0.00	0.00±0.00
	-0.2	88.0±2.1	11.1±0.7	4.5±0.2	0.0±0.0	3.48±0.08	0.44±0.03	0.18±0.01	0.00±0.00
	-0.3	97.9±1.9	2.3±0.1	1.2±0.1	0.0±0.0	5.91±0.12	0.14±0.01	0.07±0.01	0.00±0.00
	-0.4	98.3±1.0	3.1±0.2	1.3±0.1	0.0±0.0	7.54±0.08	0.24±0.01	0.10±0.00	0.00±0.00
	-0.6	94.7±2.0	2.0±0.1	0.4±0.0	0.0±0.0	10.34±0.30	0.22±0.01	0.04±0.00	0.00±0.00
Bi 2 nm /GaN/Si	0.2	10.0±1.3	62.7±3.8	17.5±6.1	0.0±0.0	0.03±0.00	0.18±0.01	0.05±0.02	0.00±0.00
	0	10.4±1.0	72.3±2.7	7.5±0.8	0.0±0.0	0.07±0.01	0.47±0.02	0.05±0.00	0.00±0.00
	-0.2	11.9±2.1	75.0±1.5	10.8±1.4	0.0±0.0	0.19±0.03	1.19±0.02	0.17±0.02	0.00±0.00
	-0.3	15.4±1.2	69.7±4.9	11.3±0.9	0.0±0.0	0.37±0.03	1.68±0.12	0.27±0.02	0.00±0.00
	-0.4	15.2±1.2	74.0±3.6	11.7±0.4	0.0±0.0	0.52±0.04	2.52±0.12	0.40±0.01	0.00±0.00
	-0.6	12.6±3.1	79.5±3.7	9.9±0.6	0.0±0.0	0.75±0.19	4.72±0.22	0.59±0.04	0.00±0.00

Table S2. Performance and reaction condition comparison of photocathodes and Bi-based electrocatalysts for CO_2 reduction reaction to HCOOH from recent literature.

Photocathodes or (Electrocatalysts)	Catalysts	Conditions	FE_{HCOOH} (%)	j_{HCOOH} (mA/cm^2)	Ref
GaN NWs/p-n^+ Si	Bi NPs	0.1 M $KHCO_3$, -0.6 V_{RHE}	95%	10.3	This work
p-Si NWs	Sn NPs	0.1 M $KHCO_3$, -0.875 V_{RHE}	88%	~4	1
NiO/GaN NWs /p-n^+ Si	NphN-$Ru(CP)_2^{2+}$ -RuCt	0.05 M $NaHCO_3$, -0.25 V_{RHE}	69%	1.1	2
p-n^+ Si	SnO_2 NWs	0.1 M $KHCO_3$, -0.4 V_{RHE}	59.2%	~10	3
GaN NWs/p-n^+ Si	Sn NPs	0.1 M $KHCO_3$, -0.53 V_{RHE}	76.9%	~11	4
Co_3O_4	$Ru(bpy)_2$dppz	0.1 M $NaHCO_3$, -0.6 V_{NHE}	86%	~6.5	5
p-Si NWs	Nanotube-derived Bi	0.5 M $KHCO_3$, -0.4 V_{RHE}	96%	~8	6
p-Si	Bi	0.5 M $KHCO_3$, -0.32 V_{RHE}	94%	~4	7
(Electrocatalyst)	Bi nanosheet	0.1M $KHCO_3$ -0.85 V_{RHE}	85%	6.2	8
(Electrocatalyst)	Bi curved nanostructure	0.5 M $KHCO_3$ -0.9 V_{RHE}	92%	15	9
(Electrocatalyst)	Bi nanoflake	0.1M $KHCO_3$ -0.8 V_{RHE}	~100%	~3	10
(Electrocatalyst)	Ultrathin Bi nansheet	0.5 M $NaHCO_3$ -0.8 V_{RHE}	89%	3.95	11
(Electrocatalyst)	Sulfide-derived bismuth	0.5 M $NaHCO_3$ -0.75 V_{RHE}	84%	5	12
(Electrocatalyst)	Bismuth oxide derivative	0.5 M $KHCO_3$ -0.9 V_{RHE}	91%	8	13
(Electrocatalyst)	Bi dendrite	0.5 M $KHCO_3$ -0.74 V_{RHE}	89%	2.7	14

References

1. S. K. Choi, U. Kang, S. Lee, D. J. Ham, S. M. Ji and H. Park, *Adv. Energy Mater.*, 2014, **4**, 1301614.
2. B. Shan, S. Vanka, T.-T. Li, L. Troian-Gautier, M. K. Brennaman, Z. Mi and T. J. Meyer, *Nat. Energy*, 2019, **4**, 290-299.
3. K. R. Rao, S. Pishgar, J. Strain, B. Kumar, V. Atla, S. Kumari and J. M. Spurgeon, *J. Mater. Chem. A*, 2018, **6**, 1736-1742.

4. B. Zhou, X. Kong, S. Vanka, S. Cheng, N. Pant, S. Chu, P. Ghamari, Y. Wang, G. Botton and H. Cuo, *Energy Environ. Sci.*, 2019, **12**, 2842-2848.
5. X. Huang, Q. Shen, J. Liu, N. Yang and G. Zhao, *Energy Environ. Sci.*, 2016, **9**, 3161-3171.
6. Q. Gong, P. Ding, M. Xu, X. Zhu, M. Wang, J. Deng, Q. Ma, N. Han, Y. Zhu and J. Lu, *Nat. Commun.*, 2019, **10**, 1-10.
7. P. Ding, Y. Hu, J. Deng, J. Chen, C. Zha, H. Yang, N. Han, Q. Gong, L. Li and T. Wang, *Mater. Today Chem.*, 2019, **11**, 80-85.
8. T. Gao, X. Wen, T. Xie, N. Han, K. Sun, L. Han, H. Wang, Y. Zhang, Y. Kuang and X. Sun, *Electrochim. Acta*, 2019, **305**, 388-393.
9. P. Lu, D. Gao, H. He, Q. Wang, Z. Liu, S. Dipazir, M. Yuan, W. Zu and G. Zhang, *Nanoscale*, 2019, **11**, 7805-7812.
10. S. Kim, W. J. Dong, S. Gim, W. Sohn, J. Y. Park, C. J. Yoo, H. W. Jang and J.-L. Lee, *Nano Energy*, 2017, **39**, 44-52.
11. P. Su, W. Xu, Y. Qiu, T. Zhang, X. Li and H. Zhang, *ChemSusChem*, 2018, **11**, 848-853.
12. Y. Zhang, F. Li, X. Zhang, T. Williams, C. D. Easton, A. M. Bond and J. Zhang, *J. Mater. Chem. A*, 2018, **6**, 4714-4720.
13. P. Deng, H. Wang, R. Qi, J. Zhu, S. Chen, F. Yang, L. Zhou, K. Qi, H. Liu and B. Y. Xia, *ACS Catal.*, 2019, **10**, 743-750.
14. J. H. Koh, D. H. Won, T. Eom, N.-K. Kim, K. D. Jung, H. Kim, Y. J. Hwang and B. K. Min, *ACS Catal.*, 2017, **7**, 5071-5077.